ENCIT 2018

ABCM Associação Brasileira de Engenharia e Ciências Mecânicas

17th Brazilian Congress of Thermal Sciences and Engineering
November 25th-28th, 2018, Águas de Lindóia, SP, Brazil

# ENCIT-2018
# HIGH FIDELITY SIMULATION AND PROPER ORTHOGONAL DECOMPOSITION OF A PLUNGING AIRFOIL IN DEEP DYNAMIC STALL

**Brener d'Lélis**
**William R. Wolf**
Faculdade de Engenharia Mecânica, Universidade Estadual de Campinas, Rua Mendeleyev 200, Campinas,SP
brener.lelis@gmail.com
wolf@fem.unicamp.br

***Abstract.*** *High fidelity simulations are performed to study deep dynamic stall of a SD7003 airfoil in plunging motion. The numerical computations employ sixth-order compact schemes for spatial derivatives, interpolation and filtering on a staggered grid. The SD7003 profile undergoes a plunge motion at* $Re = 60000$*,* $Ma = 0.1$*, static angle of attack* $\alpha = 8\,\mathrm{deg}$ *. and reduced frequency* $k = 0.5$*. This configuration was adopted due to availability of data from experiments and simulations. Good agreement with previous work is found, especially in the earlier stages of the dynamic stall vortex (DSV) formation. Finally, proper orthogonal decomposition analysis (POD) of the simulated flow is performed. Only a few modes are necessary to recover the main features of the aerodynamic loading, showing promising results for creating a reduced order model of this type of flow.*

***Keywords:*** *High fidelity simulation, proper orthogonal decomposition, plunge motion, dynamic stall, SD7003 airfoil*

## 1. INTRODUCTION

The study of dynamic stall finds application in aeronautical engineering, especially in military applications of maneuvering aircraft and in helicopter flight McCroskey (1982). Such applications have been extensively studied in the literature for high Reynolds numbers applications. However, low Reynolds number investigations of dynamic stall are a recent topic of research. Unsteady low Reynolds number flows are found in several natural flying systems; for example, birds and insects. Moreover, these flow conditions are also relevant for modern engineering devices such as small unmanned air vehicles and micro air vehicles. For all these cases, the low Reynolds numbers are due to the small characteristic length scales and/or the low characteristic speeds involved in such flows (Shyy, 2008). In some cases, these flow fields can be characterized by extensive regions of laminar flow including hydrodynamic instabilities, by the onset of laminar separation bubbles, by laminar-turbulent transition zones, and by fully turbulent zones.

Unsteady flows over plunging and pitching airfoils with large excursions in effective angle of attack exhibit the phenomenon termed dynamic stall, a process characterized by unsteady separation and by the formation of large-scale leading-edge and trailing-edge vortices, which exert difficult-to-predict variations in aerodynamic loads. Comprehensive reviews of this phenomenon, first discovered and studied extensively in the context of helicopter rotor blades, have been given by (McCroskey, 1982), (Carr, 1988) and (Ekaterinaris and Platzer, 1998).

For the case of flapping wings, as well as for severe impinging gusts, the highly unsteady forcing induces the formation of dynamic-stall and leading-edge vortex structures whose evolution and interaction with the aerodynamic surfaces have a significant impact on flight stability and performance. As previously discussed, much has been studied and learned about these unsteady flow features. However, several questions remain open for dynamic stall conditions at low Reynolds numbers. For example, we would like to improve our understanding on the important dynamic features involved in fully separated small-scale flows under dynamic stall. For these configurations, it is important to develop reduced order models (ROMs) that recover the important dynamics of the flow. With such ROMs, we will be able to investigate the implications of dynamic stall on flight efficiency and understand the role of the parameters involved in the flows. Then, we will be able to perform flow control for the design of more efficient engineering devices.

Reliable reduced order models of flows under dynamic stall need to be constructed based on accurate data extracted from high-fidelity experiments and simulations. High-fidelity simulations can provide an abundance of data with both spatial and temporal high resolution and is, therefore, the method of choice in this work. Several two-dimensional computational studies are available in the literature regarding dynamic stall under laminar, transitional, and turbulent conditions (Ekaterinaris and Platzer, 1998), (Visbal and Shang, 1989), (Visbal, 1991), (Choudhuri *et al.*, 1994), (Visbal, 1990), (Radespiel *et al.*, 2007). For high Reynolds number flows, these approaches have traditionally employed a hierarchy of

turbulence models augmented in some instances with empirical transition predictions.

In the present work, we employ implicit large eddy simulations (ILES) to study the flow physics of deep dynamic stall over a plunging SD7003 airfoil profile. Our numerical methodology makes use of staggered grids to represent the configuration of interest. The current ILES approach is based on a sixth-order compact scheme for the spatial derivatives. Interpolation between the staggered grids is also performed by a sixth-order compact scheme. In order to maintain stability of the numerical method, a sixth-order compact low-pass filter is applied to the solutions. A hybrid implicit-explicit framework is used to integrate the equations in time. Here, a third order low storage Runge Kutta scheme is combined with a modified Beam & Warming scheme (Nagarajan, 2004). The former is applied on regions away from the wall while the latter is used in the proximity of the wall regions.

In the present study, the flow conditions of deep dynamic stall have a reduced frequency of $k = \pi f L/U_\infty = 0.5$, where $f$ is the plunging frequency, $L$ is the chord of the SD7003 airfoil and $U_\infty$ is the reference free stream velocity. The amplitude of motion is set as $h_o/L = 0.5$ with a static angle of attack $\alpha = 8°$. The chord Reynolds number based on the freestream velocity is $Re = 60000$ and the freestream Mach number is $Ma = 0.1$. This flow condition is relevant for MAV applications. This case was selected based on the availability of results from high fidelity simulations (Visbal, 2011) and experimental particle image velocimetry (PIV) data (Kang *et al.*, 2009), (Baik *et al.*, 2009), (Ol *et al.*, 2009). Proper orthogonal decomposition of the current flow is performed to provide a better understanding of the important dynamics in the present flow configuration. We expect that such analysis will give further insight on the identification of coherent structures in this kind of flow, and on the construction of reduced order models for flow control strategies in dynamic stall.

## 2. METHODOLOGY

### 2.1 Governing Equations

To simulate a moving airfoil, the weakly conservative form of the unfiltered Navier-Stokes equations in a non-inertial frame are solved. In this form, source terms emerge from the grid curvature and frame movement. These equations have been used before by (Warsi *et al.*, 1978) and (Yamamoto and Daiguji, 2001). For simulations of turbulent flows, these equations have been used by (Orlandi, 1989) and (Choi, 1992) in DNS and by (Yang and Voke, 2001) for LES. Additionally, all terms are solved in contravariant form to allow the use of a curvilinear coordinate $\{\xi^1, \xi^2, \xi^3\}$. For a frame of reference which moves only in a translating way, the equations reduce to

$$\frac{\partial}{\partial t}(\sqrt{g}\rho) + \frac{\partial}{\partial \xi^i}(\sqrt{g}\rho u^i) = 0\,, \tag{1}$$

$$\frac{\partial}{\partial t}(\sqrt{g}\rho u^i) + \frac{\partial}{\partial \xi^j}\left[\sqrt{g}\left(\rho u^i u^j - \tau^{ij} + g^{ij}p\right)\right] + \left\{ \begin{matrix} i \\ jk \end{matrix} \right\} \sqrt{g}\Big(\rho u^k u^j + g^{jk}p - \tau^{kj}\Big) = \sqrt{g}\rho \ddot{h}^i\,, \tag{2}$$

and

$$\frac{\partial}{\partial t}(\sqrt{g}E) + \frac{\partial}{\partial \xi^j}\left\{\sqrt{g}\left[(E+p)u^j - \tau^{ij}g_{ik}u^k - \frac{\kappa}{Re\,Pr}g^{ij}\frac{\partial T}{\partial \xi^i}\right]\right\} = \rho\sqrt{g}(h^j + u^j)g_{jp}\ddot{h}^p\,. \tag{3}$$

The set of equations above represent the continuity equation, momentum equations and the energy equation. In order to close this system of equations the following relations are written

$$E = \frac{p}{\gamma - 1} + \frac{1}{2}\rho u^i g_{ij} u^j + \frac{1}{2}\rho \dot{h}^i g_{ij}\dot{h}^i\,, \tag{4}$$

$$\tau^{ij} = \frac{\mu}{Re}\left(g^{jk}u^i{}_{|k} + g^{ik}u^j{}_{|k} - \frac{2}{3}g^{ij}u^k{}_{|k}\right)\,, \tag{5}$$

and

$$h = h_o sin(kt)\,. \tag{6}$$

Here, $\rho$ represents the density, $u^i$ the i-th component of the contravariant velocity vector and $p$ is the pressure. The term $\epsilon$ is the Levi-Civita symbol, $h$ is the frame's position, $E$ is the total energy, $\mu$ is the dynamic viscosity and $T$ is the temperature. The dots represent temporal derivatives of the frame's position, i.e., frame velocity and acceleration. The quantities just mentioned are non-dimensionalized by freestream quantities such as density $\rho_\infty$ and speed of sound $c_\infty$. The length scales are made non-dimensional by the airfoil chord $L$. In the equations above, the covariant and contravariant metric tensors are described, respectively, as

$$g_{ij} \triangleq \frac{\partial x^k}{\partial \xi^i}\frac{\partial x^k}{\partial \xi^j}\,, \tag{7}$$

$$g^{ij} \triangleq \frac{\partial \xi^i}{\partial x^k}\frac{\partial \xi^j}{\partial x^k}\,, \tag{8}$$

and

$$g = |g_{ij}| = \left(\frac{\partial x^i}{\partial \xi^j}\right)^2 \tag{9}$$

More details about the present formulation can be found in (Aris, 1989).

### 2.2 Numerical Procedure

A compact sixth-order finite difference scheme constructed for a staggered grid is used to calculate all spatial derivatives. For any scalar quantity $f_i$, a tridiagonal system is solved as

$$\alpha f'_{i-1} + f'_i + \alpha f'_{i+1} = b\frac{f_{i+3/2} - f_{i-3/2}}{3\Delta x} + a\frac{f_{i+1/2} - f_{i-1/2}}{\Delta x}\,, \tag{10}$$

where $\alpha = 9/62$, $a = \frac{3}{8}(3 - 2\alpha)$ and $b = \frac{1}{8}(-1 + 22\alpha)$. Close to the boundaries, a numerical sponge is used to damp acoustic waves and, at the inlet and outlet boundaries, a Riemann invariant transformation is implemented as the far field condition. The derivatives of the inviscid fluxes are obtained by forming the fluxes between the grid nodes and differentiating each component with the above formula. Viscous terms are obtained by first computing the derivatives of the primitive variables in their respective locations. The components of the viscous fluxes are then constructed at each node and differentiated by a second application of the same scheme. The airfoil movement is added through the source terms shown in the formulation section.

To minimize errors from non-resolved scales, a sixth-order compact low-pass filter is applied according to

$$\bar{\alpha}\bar{f}_{i-1} + \bar{f}_i + \bar{\alpha}\bar{f}_{i+1} = f_i + \frac{b}{2}(f_{i+1} + f_{i-1}) + \frac{c}{2}(f_{i+2} + f_{i-2}) + \frac{d}{2}(f_{i+3} + f_{i-3})\,. \tag{11}$$

In the equation above, $a = \frac{1}{16}(11 + 10\bar{\alpha})$, $b = \frac{1}{32}(15 + 34\bar{\alpha})$, $c = \frac{1}{16}(-3 + 6\bar{\alpha})$ and $d = \frac{1}{32}(1 - 2\bar{\alpha})$. The $\bar{\alpha}$ parameter can have values in the range $[-0.5, 0.5]$, with $-0.5$ implying in the most severe filter and $0.5$ in "turning off" the filter. In the current simulations, $\bar{\alpha} = 0.46$ is used, which implies in a very small amount of filtering. The filter is applied after each time sub-step for the Runge Kutta scheme and after each time-step of the modified Beam & Warming scheme.

Due to the staggered grid, interpolations are necessary to evaluate properties in the specific grid locations. To maintain the overall high-order of the schemes, a sixth-order interpolation based on finite differences is used according to

$$\tilde{\alpha}\tilde{f}_{i-1} + \tilde{f}_i + \tilde{\alpha}\tilde{f}_{i+1} = \frac{b}{2}(f_{i+3/2} + f_{i-3/2}) + \frac{a}{2}(f_{i+1/2} + f_{i-1/2})\,, \tag{12}$$

where $\tilde{\alpha} = 3/10$, $a = \frac{1}{8}(9 + 10\tilde{\alpha})$ and $b = \frac{1}{8}(6\tilde{\alpha} - 1)$. More details about the finite difference schemes used for derivation, filtering and interpolation can be found in (Lele, 1992) and (Nagarajan, 2004). All of the schemes discussed are implemented with periodic boundary conditions in the streamwise and spanwise directions.

Two time-marching methods are utilized to advance solution in time. A compact storage third order Runge-Kutta scheme is used to advance the solution of the outer grid, away from solid walls. In the inner grid, an implicit time marching scheme with approximate factorization derived from a Beam & Warming method is used. More details about those schemes can be found in (Nagarajan, 2004).

## 3. PRELIMINARY RESULTS

Three numerical simulations are performed to identify the influence of mesh refinement in the simulated flows. Only the results from the second most refined are shown in this extended abstract. The simulation parameters are found in Tab. 1 and Fig. 1 shows the grid with every other line, both in the streamwise and wall-normal directions. The current grid is generated with $70\%$ of the surface points located in the suction side of the airfoil. This procedure is employed since the finest dynamic scales of the turbulent flow will be formed along this region. Due to the favorable pressure gradients in the pressure side of the airfoil, the flow will be laminar along the entire cycle of the plunging motion. The trailing edge of the SD7003 airfoil is rounded in the current simulations with an arc of radius $r/L = 0.0004$. This procedure is required for keeping the smoothness of the metric terms.

Table 1: Simulation parameters

| Cycles | Grid ($x \times y \times z$ ) | Span | Reynolds | Mach | Static Angle of Attack | $\Delta t^* = \frac{\Delta t U_\infty}{L}$ |
|---|---|---|---|---|---|---|
| 5 | $441 \times 139 \times 64$ | 0.4 | $60,000$ | 0.1 | $8°$ | 0.00008 |

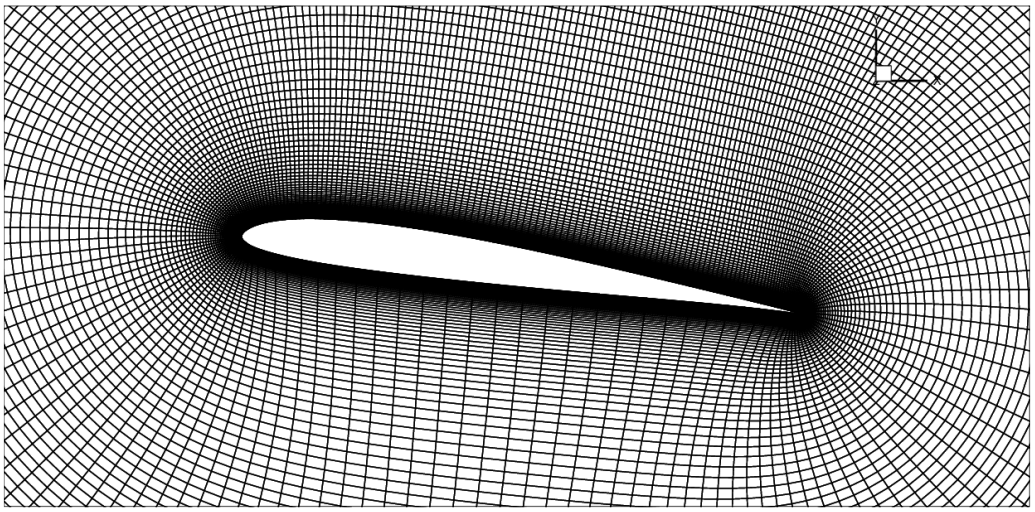

Figure 1: Grid used to perform the simulation (only every other grid point is shown here).

The plunge motion implicates in an effective angle of attack in the range of $-6° \leq \alpha_{eff} \leq 22\,\mathrm{deg}$. Due to transient fluctuations, only 4 cycles are used in the calculation of the statistics. In order to facilitate visualization, a phase angle $\phi$ is used to describe the position of the airfoil. At $\phi = 0°$ the airfoil has no velocity in the y-direction and is at the top-most position of the plunge motion. At $\phi = 90°$ it has the highest velocity in the y-direction downwards and, at $\phi = 180°$, it has no velocity and is at the bottom-most position of the plunge motion. Finally, at $\phi = 270°$ it has the highest velocity in the y-direction upwards. An schematic of the current plunging motion is shown in Fig. 2

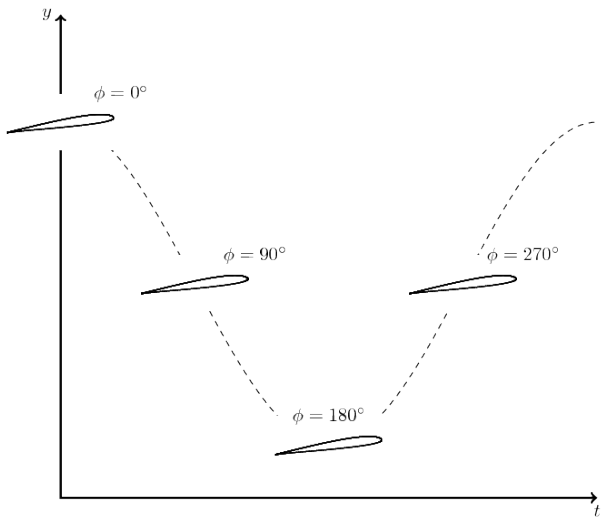


Figure 2: Airfoil position according to the phase angle $\phi$.

During the down-stroke, instabilities begin to form in the suction side of the airfoil as shown in Fig. 3a. As the movement continues, these instabilities grow and eventually break into finer structures, creating a transitional regime. While this happens, the main leading-edge vortex (LEV) begins to form as shown in Fig. 3b. Then, the LEV is transported by flow through the suction side (Fig. 3c) of the airfoil, increasing the overall lift load and creating a nose-down pitch moment. As the LEV gets closer to the trailing edge, a trailing edge vortex (TEV) forms and "pushes" the LEV away from the airfoil (Fig. 3d). When this happens, an oscillation in the pitching moment can be observed. As the motion continues, the TEV is also convected away from the airfoil and re-laminarization starts to occur in the leading edge (Fig. 3e). As

the airfoil moves upwards, the laminar region begins to grow (Fig. 3f) until the whole boundary-layer is laminar (Fig. 3g) and a Kelvin-Helmholtz type instability forms leading to periodic shedding. Since the main focus of this work is to study dynamic stall, latter phase angles are not shown.

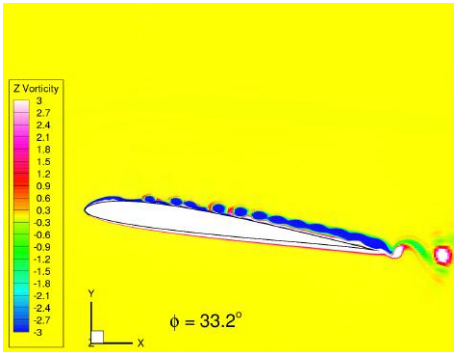


(a) Formation of instabilities.

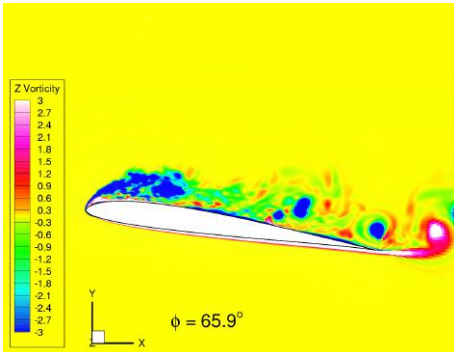


(b) Formation of the leading-edge vortex.

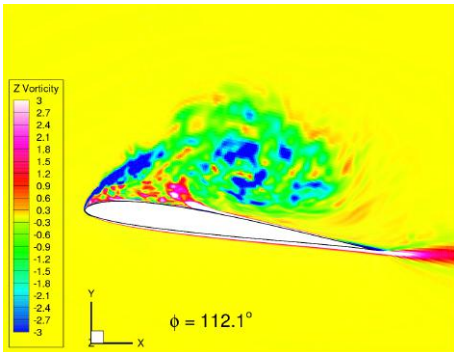


(c) Leading-edge vortex being convected.

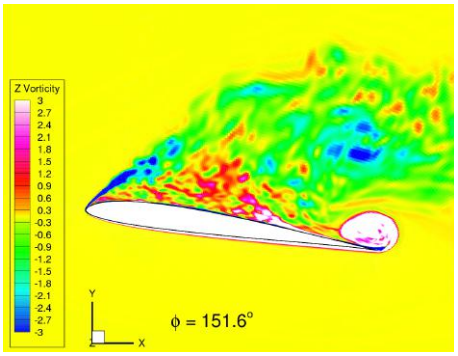


(d) Formation of the trailing edge vortex

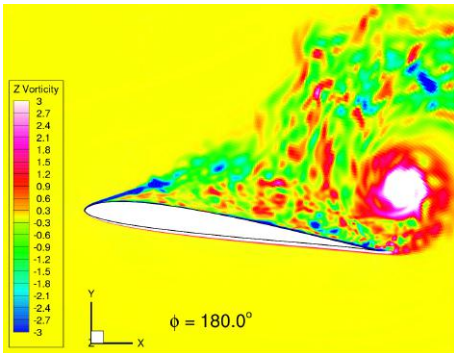


(e) Flow at the leading edge begins to re-laminarize.

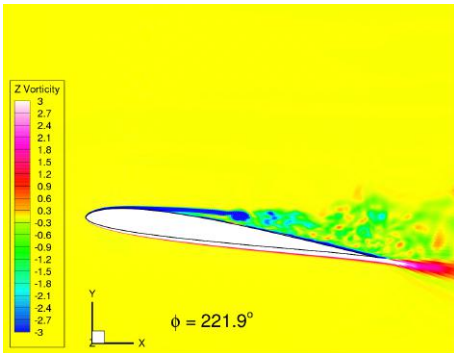


(f) Laminar and turbulent features at the suction side.

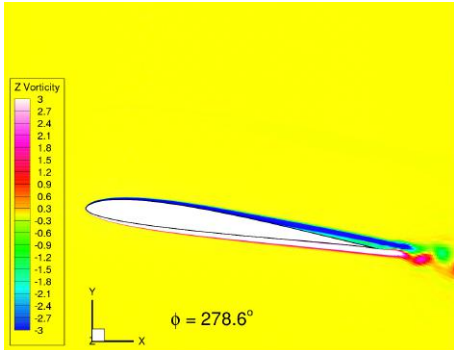


(g) The entire flow around the airfoil has become laminar again.

Figure 3: Z vorticity contours at several phase angles for spanwise averaged solutions.

Comparison between aerodynamic loads found in (Visbal, 2011) are shown in Fig. 4. To compute these statistics, first,

a spanwise averaging is performed followed by a phase averaging. The overall curves are in good agreement with the literature reference. It should be mentioned that a new simulation with a finer mesh is currently being run and is expected to provide even better results than those shown here.

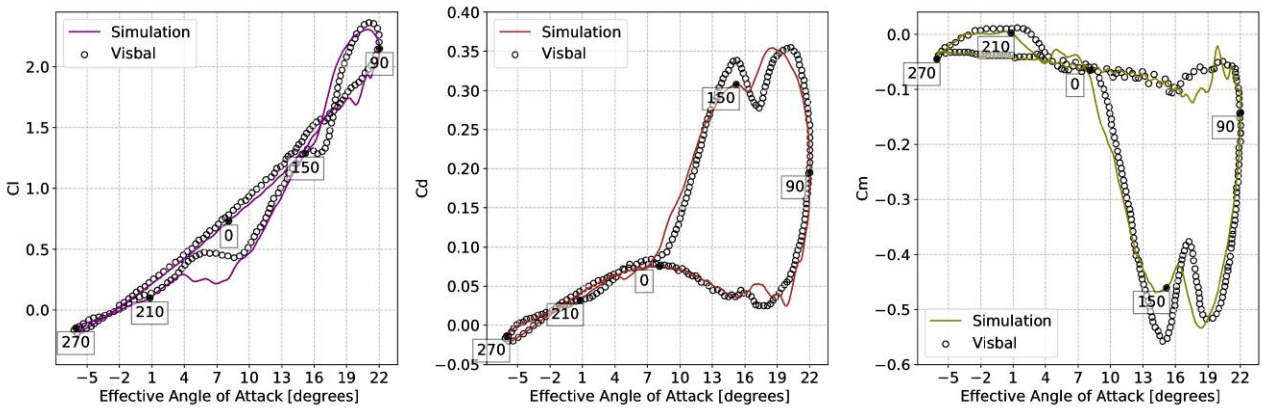


Figure 4: Comparison between aerodynamic loads.

Iso-surfaces of Q-criterion are shown in Fig. 5. It can be seen that at different stages, the flow can be completely laminar, transitional or turbulent. Depending on the flow states, different coherent structures can be observed. When the flow is fully separated, the analysis of such coherent flow structures becomes compromised since finer scales dominate the visualization. The most energetic structures should have larger spatial scales and should dominate the dynamics of the present flow. A simple visualization in terms of Q-criterion is not sufficient for such analysis and, therefore, more advanced treatments should be employed for the investigation of the turbulent coherent structures.

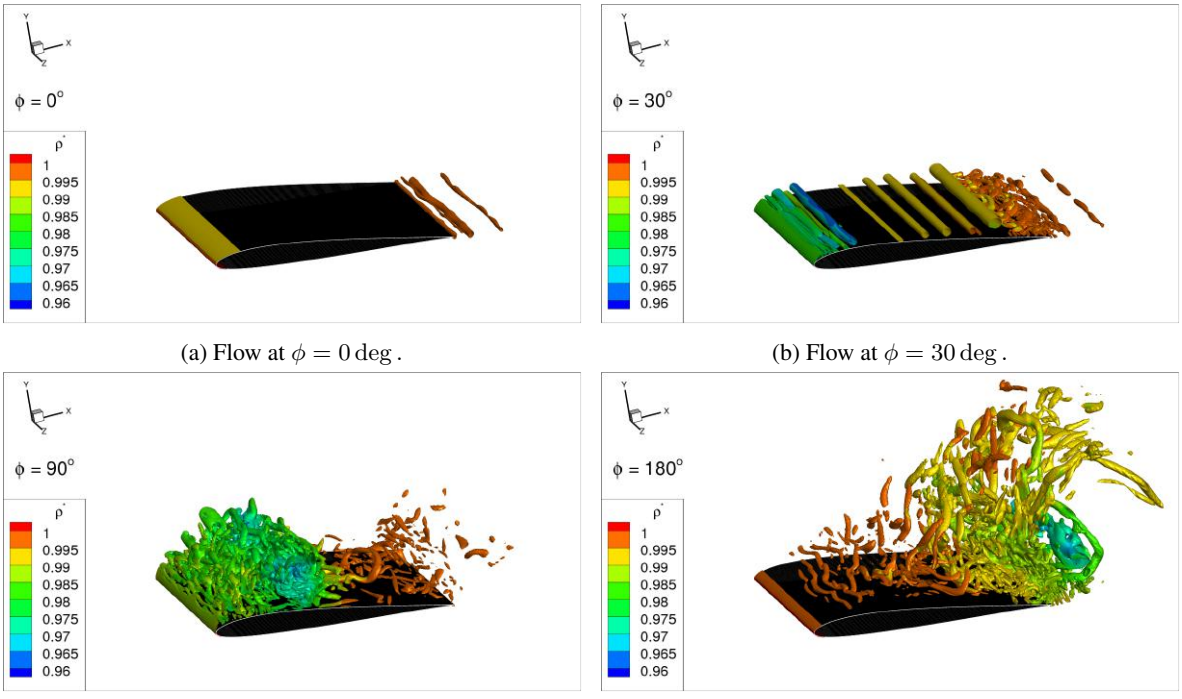


(a) Flow at $\phi = 0\,\mathrm{deg}$.

(b) Flow at $\phi = 30\,\mathrm{deg}$.

(c) Flow at $\phi = 90\,\mathrm{deg}$.

(d) Flow at $\phi = 180\,\mathrm{deg}$.

Figure 5: Iso-surfaces of Q criterion for $Q = 5$ colored by density at different instants of the plunge motion.

A POD analysis is performed using the spanwise averaged solutions of the flow fields to analyze the dynamics of the most energetic flow structures. The current POD analysis employs a pressure norm for the construction of the correlation matrix. Here, the main goal is to capture the loadings created by the dynamic stall vortex. The first POD spatial modes are displayed for the x-momentum (Fig. 6a), y-momentum(Fig. 6b) and pressure (Fig. 7). As can be seen in these figures, large scale structures are present in the first POD modes. These structures are mainly related with the transport of the dynamic stall vortex over the suction side of the airfoil.

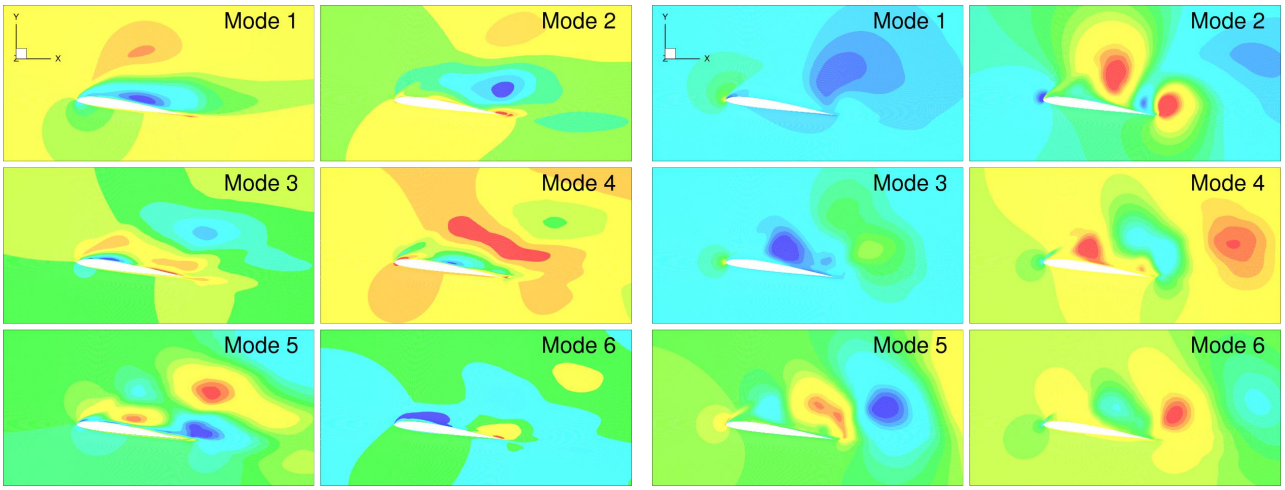


(a) X momentum modes. (b) Y momentum modes.

Figure 6: Momentum modes.

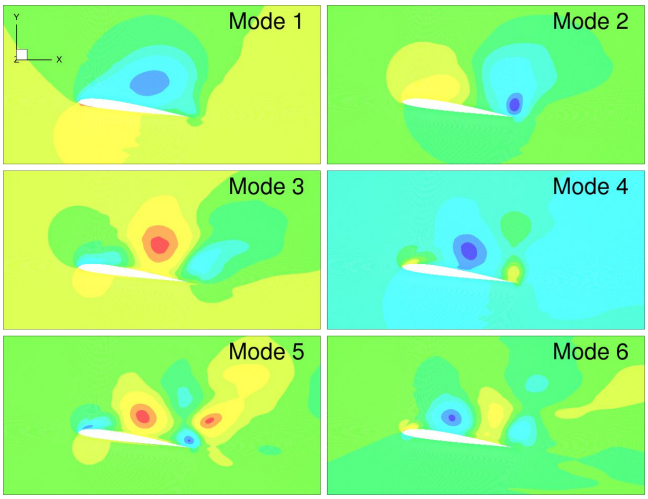


Figure 7: Pressure modes.

The normalized singular values and their summation are plotted in Fig. 8. When performing the analysis with the conditions just mentioned, $1.34\%$ of the modes have $54.59\%$ of the total solution energy. However, because of the logarithmic shape of the singular values summation curve, $7.68\%$ of modes are necessary to recover $80.00\%$ of the solution energy. Also, it can be seen that there is a poor correlation between modes, which is related to the lack of symmetry in the current analysis. In general, POD modes are paired for spatially symmetric periodic flows. Here, the plunging motion leads to a different configuration where the POD modes are poorly paired.

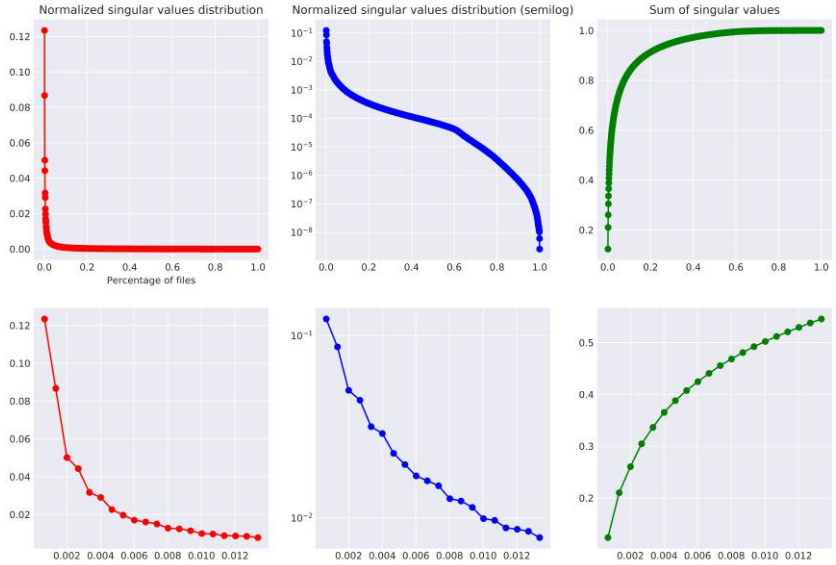


Figure 8: Distribution of singular values.

Performing a reconstruction of the solution with only 20 modes returns the aerodynamic loads curves shown in Fig. 9. The main dynamics of the dynamic stall vortex is captured but discrepancies are observed specially in the laminar stages of the plunge motion. The main deviation occurs in the $cd$ curve when the drag contribution from viscosity has a significant influence ($270° \leq \phi \leq 390°$).

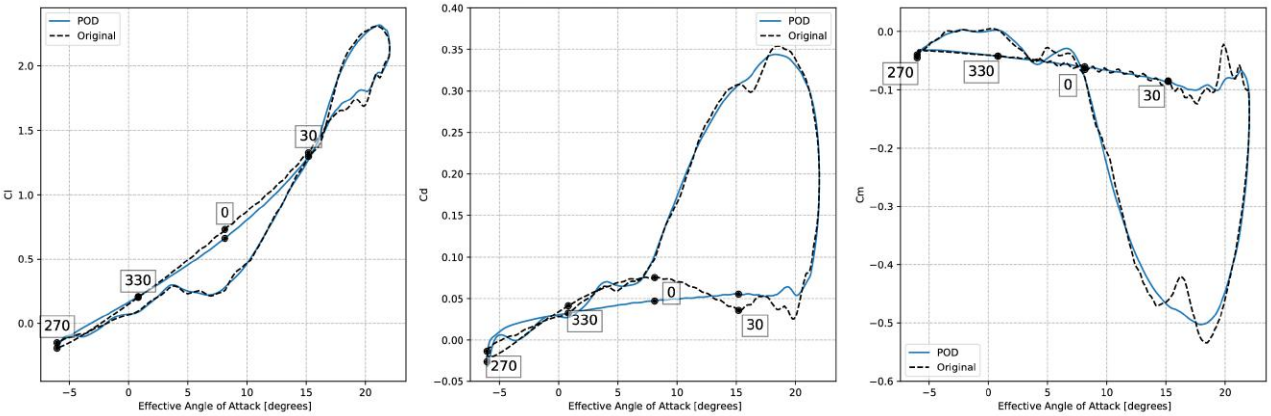


Figure 9: Comparison of aerodynamic loads between original data and POD reconstruction.

## 4. Conclusions/Additions

High fidelity simulations using an ILES approach are performed for a SD7003 profile in plunging motion. Results from the simulations are compared to previous work with the same parameters, showing good agreement. As the instabilities arise after the beginning of the down-stroke, a LEV starts to form and grow. After reaching a given size, it is convected through the suction side of the airfoil, increasing both lift and drag while decreasing pitching moment so that a nose-down moment is created. When close to the trailing edge, the LEV is "pushed" by a TEV recently formed, which briefly stops the loss of lift and creates oscillations in drag and pitching moment. After the TEV is also convected away from the airfoil, the shear layer starts to become laminar and the whole process starts again. It is interesting to notice that, even with a low-dissipation and high-order numerical schemes, there are a significant variation of aerodynamic loads between cycles. In this way, simulating more cycles should improve statistics.

A POD analysis is performed in the spanwise averaged flowfields. Despite using only about $1\%$ of the available modes, which recover about $55\%$ of the flow energy, the reconstructed aerodynamic loads agree very well with those

of the original data, except when the shear-layer is predominantly laminar. A spectral proper orthogonal decomposition (SPOD) is being implemented and is expected to provide better reconstructions of the flowfield. Also, a new simulation is being performed for a refined mesh with the expectancy of providing even better data to perform the reconstructions and validate the numerical tools used in this work.

## 5. ACKNOWLEDGEMENTS

The authors acknowledge the financial support received from Fundação de Amparo à Pesquisa do Estado de São Paulo, FAPESP, under Grants No. 2016/24504-6. We thank CENAPAD-SP and SDUMONT-LNCC for the computational resources provided.

## 6. REFERENCES

Aris, R., 1989. *Vectors, Tensors, and the Basic Equations of Fluid Mechanics*. Dover Publications.

Baik, Y.S., Rausch, J.M., Bernal, L.P. and Ol., 2009. "Experimental investigation of pitching and plunging airfoils at reynolds number between 1 x $10^4$ and 6 x $10^4$". In *AIAA Paper*.

Carr, L., 1988. "Progress in analysis and prediction of dynamic stall". *Journal of Aircraft*, Vol. 25, pp. pp. 6–17.

Choi, H., 1992. *Turbulent Drag Reduction: Studies of Feedback Control and Flow Over Riblets*. Ph.D. thesis, Stanford University.

Choudhuri, P.G., Knight, D.D. and Visbal, M.R., 1994. "Two-dimensional unsteady leading-edge separation on a pitching airfoil". *AIAA Journal*, Vol. 32, No. 4, p. pp. 673–681.

Ekaterinaris, J. and Platzer, M., 1998. "Computational prediction of airfoil dynamic stall". *Progress in Aerospace Sciences*, Vol. 33, p. pp. 759–846.

Kang, C.K., Baik, Y.S., Bernal, L.P., V., M. and Shyy, W., 2009. "Fluid dynamics of pitching and plunging airfoils for reynolds number between 1 x $10^4$ and 6 x $10^4$". In *AIAA Paper*.

Lele, S.K., 1992. "Compact finite difference schemes with spectral-like resolution". *Journal of Computational Physics*, Vol. 103, p. pp. 16–42.

McCroskey, W.J., 1982. "Unsteady airfoils". *Annual Review of Fluid Mechanics*, Vol. 14, pp. pp. 285–311.

Nagarajan, S., 2004. *Leading Edge Effects in Bypass Transition*. Ph.D. thesis, Stanford University.

Ol, V., M., Bernal, L.P., Kang, C.K. and Shyy, W., 2009. "Shallow and deep dynamic stall for flapping low reynolds number airfoils". *Experiments in Fluids*, Vol. 46, p. pp. 883–901.

Orlandi, P., 1989. "A numerical method for direct simulation of turbulence in complex geometries". *CTR Annual Research Briefs*, p. pp. 215–229.

Radespiel, R., Windte, J. and Scholz, U., 2007. "Numerical and experimental flow analysis of moving airfoils with laminar separation bubbles". *AIAA Journal*, Vol. 45, No. 6, p. pp. 1346–1356.

Shyy, W., 2008. *Aeroynamics of Low Reynolds Number Flyers*. Cambridge University Press, New York.

Visbal, M.R., 1990. "Dynamic stall of a constant-rate pitching airfoil". *Journal of Aircraft*, Vol. 27, No. 5, pp. pp. 400–407.

Visbal, M.R., 1991. "On the formation and control of the dynamic stall vortex on a pitching airfoil". In *AIAA Paper*.

Visbal, M.R., 2011. "Numerical investigation of deep dynamic stall of a plunging airfoil". *AIAA Journal*, Vol. 49, No. 10, pp. pp. 2152–2170.

Visbal, M.R. and Shang, J.S., 1989. "Investigation of the flow structure around a rapidly pitching airfoil". *AIAA Journal*, Vol. 27, No. 8, p. pp. 1044–1051.

Warsi, Z.U.A., Devarayalu, K. and Thompson, J.F., 1978. "Numerical solution of the navier-stokes equations for arbitrary blunt bodies in supersonic flows". *Numerical Heat Transfer*, Vol. 1, p. pp. 499–516.

Yamamoto, S. and Daiguji, H., 2001. "A numerical method for the transonic cascade flow problem". *Computers and Fluids*, Vol. 19, p. pp. 461–477.

Yang, Z. and Voke, 2001. "Large-eddy simulation of boundary-layer separation and transition at a change of surface curvature". *Journal of Fluid Mechanics*, Vol. 439, p. pp. 305–333.

## 7. RESPONSIBILITY NOTICE

The authors are the only responsible for the printed material included in this paper.